Large Laboratory Simulator of Natural Rainfall: From Drizzle to Storms

(Article begins on next page)

11 February 2024

Article

Large Laboratory Simulator of Natural Rainfall: From Drizzle to Storms

Roberto Bosio *, Andrea Cagninei and Davide Poggi

Department of Environment, Land and Infrastructure Engineering (DIATI), Politecnico di Torino, Corso Duca degli Abruzzi 24, 10129 Torino, Italy
* Correspondence: roberto.bosio@polito.it

Abstract: Rainfall simulators are versatile research tools that facilitate studying rain events and the many related physical phenomena. This work describes the development and validation of an indoor, large-scale rainfall simulator comprising a rain module installed 10.4 m from ground level, a redistribution screen at an adjustable distance below the rain module, and an ultra-filtered-water recirculation system. The droplet formers installed in the rain module were selected to achieve a wide range of rain intensities. The simulator was calibrated and validated using local natural rainfall data collected with a disdrometer over 30 months. The height of the rain module allows terminal velocity to be reached at ground level. At the same time, the redistribution screen and the droplet formers guarantee the wide variability of simulated rainfall in terms of intensity and the size of the drops. As a result, we show that the rain simulator, with proper calibration of the screen's position, can reproduce measured natural rainfall over a broad range of intensities with high spatial and temporal uniformity and kinetic energy.

Keywords: large-scale rainfall simulator; natural rain simulation; disdrometer

1. Introduction

Rainfall has always been challenging to investigate because of its unpredictable nature and the many complex mechanisms that govern it. Although countless steps forward have been taken, many related phenomena still need to be fully understood and require physical modelling.

Numerical cloud models can reproduce the complex dynamic and microphysical interactions in individual clouds and cloud systems, simulating various rainfall intensities and droplet sizes by incorporating different cloud parameters [1–3]. Once the characteristics of rain are known, physical models can accurately reproduce precipitation on the ground and in the lower atmosphere, allowing complex effects to be investigated in detail.

Rainfall simulators are experimental apparatuses whose main task is the accurate reproduction of natural rain. For this, several conditions must be met [4–6], such as the drop size distribution being similar to a real distribution, the achievement of terminal velocity by the formed drops, the spatial and temporal homogeneity of the produced intensity throughout the tests, as well as the ability to simulate natural events by following a recorded intensity pattern. The complete control of rainfall variables is the main advantage of rainfall simulators. Rain can be generated on demand, ensuring the accurate performance of experiments. The absence of external forcings (e.g., wind) and the control of atmospheric parameters, including temperature and humidity, ensure greater repeatability than field experiments. On the other hand, rainfall simulators are constrained by surface areas much smaller than those that characterize field experiments. Rainfall simulators were introduced in the 1930s to study soil erosion [7]. Since then, they have been adapted to case studies with a focus on splash-erosion mechanisms [7–13], surface runoff [14–16], washoff [17], and the effects of rain on the physical and chemical properties of soils [18–22], pavements [23],

and materials [24]. Depending on their ability to be moved, rainfall simulators can be divided into laboratory and field devices [6,14,16,25–27]. The small areas over which tests can be conducted are a major limitation of these systems. To date, systems capable of simulating natural rain on a large scale (wetted areas > 10 m^2), both for laboratory and field experiments, are very rare. According to [28], more than 95% of the apparatuses described in the literature cover an area less than 2 m^2.

Rainfall simulators are classified into nozzle-spraying and drop-former simulators based on the droplet generation system. Nozzle-spraying simulators require low fall heights due to the initial droplet velocity caused by the pressure in the system. By varying the pressure, they can generate polydispersed precipitation with a wide intensity range. However, they have several limitations that impact their applicability: as pressure increases, a reduction in average droplet diameter occurs [29], in contrast to what is observed in natural rain events [30]; because the systems are under pressure, the reproduction of light rainfall of low intensity is hard to achieve; and the continuous spray produced by the nozzle overpredicts the natural rainfall conditions on the ground, both in terms of droplet velocity and kinetic energy. To bypass these problems, some alternative configurations have been proposed. In particular, directing the nozzle upwards allows the initial imprinted velocity to be cancelled out [31,32], while using a rotating arm or disc distributes the jet over a wider area, thus reducing rain intensity [33,34] (but potentially causing a problem of intermittent rain on the ground).

In contrast, drop-former rainfall simulators employ needles [25,27,35], capillary tubes, or polyethene tubing [32,36]. They can generate monodispersed rainfall with no reductions in average diameter as intensities increase thanks to surface tensions that control the drop-formation process [36]. Polydispersed rain can also be reproduced by installing injectors of assorted sizes, using a breaking grid [3,14], or by combining these systems. To generate high rain intensities and realistic droplet densities, injectors must be installed in dense arrays (e.g., with 2–3 cm spacing). As droplets are generated with no velocity, they require considerable fall heights to reach terminal velocity, making these systems difficult to use outside the laboratory.

To our knowledge, no laboratory rainfall simulators can guarantee the realistic reproduction of natural rainfall properties on a large scale, over a wide range of intensity, and with high accuracy. Nevertheless, such an experimental facility would create opportunities in countless research areas, such as the simulation of erosion phenomena on a large scale, the testing of drainage pavements, the calibration and testing of sensors, the performance of washout tests on different surfaces, and the carrying out of surface-runoff and atmospheric-washout studies. Thanks to the large simulation surface areas, more robust tests could be conducted on soil erosion and washout and particle-resuspension phenomena thanks to the possibility of changing the ground surface at will. Therefore, this article describes the design and fine-tuning of a large-scale, drop-former rainfall simulator that can simulate a wide range of intensities while ensuring natural rainfall characteristics (i.e., spatial homogeneity, droplet size distribution, and kinetic energy on the ground). To this end, we compared the data acquired with a disdrometer installed outdoors with the properties of the rain generated by the rainfall simulator.

2. Materials and Methods

2.1. The Rainfall Simulator

2.1.1. Design and Measurement Devices

The rainfall simulator is housed in a 3.5 m × 4 m × 10.7 m 3-storey tower made of an aluminium TRUSS arrangement located in the Hydraulics Laboratory of the Politecnico di Torino (Italy). A group of 8 steel plates attached to 16 TRUSS support hooks secure the rain module at the top of the tower (see Figure 1a), ensuring a droplet-free fall height of about 10.4 m, which corresponds to a 98% terminal velocity for droplets with diameters less than 3 mm, according to Gunn et al. [37].
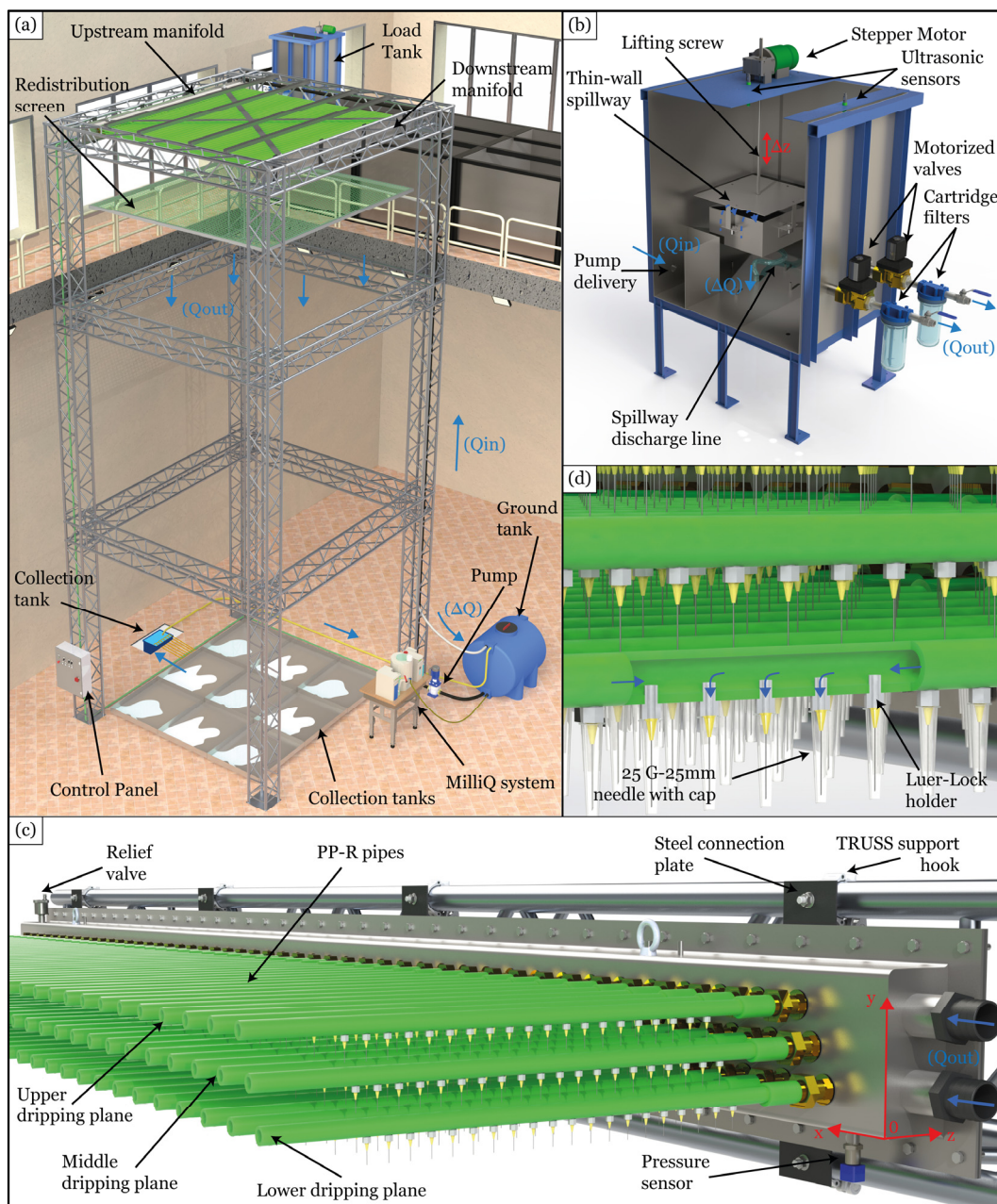
Figure 1. Overview of the experimental setup: (**a**) rendering of the rainfall simulator facility; (**b**) rendering of the load tank; (**c**) representation of the upstream manifold (the reference system for the water-head measurement is included in red), with the lower, middle, and upper dripping planes also specified; and (**d**) detailed view of the dripping system.

The functional design is based on the principle of recirculation of excess flow rates. This principle states that, under steady-state conditions, $\Delta Q = Q_{in} - Q_{out}$, with $dV/dt = 0$. A 2 m^3 PPE tank on the ground feeds a 1 m^3 stainless-steel load tank at the top of the tower through a multistage pump with a constant flow rate (Q_{in}) of 45 l/min (see Figure 1a). Two motorised valves control the flow (Q_{out}) from the load tank to the rain module. A 350 mm × 350 mm × 180 mm thin-walled spillway moved by a stepper motor controls the water level in the load tank, ensuring a constant head to the rain module by returning excess flow (ΔQ) to the ground tank. With a minimum spillway displacement of 2 mm, the water load in the rain module is precisely controlled, ensuring controlled intensity increments in the order of 0.6 mm/h.

Two ultrasonic sensors monitor the water level in the load tank and the spillway's height in real time (see Figure 1b). The water head on the needles is managed by moving the spillway and thus changing the water level in the load tank. Since the flow rates through the droplet generators vary proportionally with the water head, this system provides high control over the intensities generated, allowing level regulations at 5 mm intervals up to a maximum water head of 50 cm over the dripping plane.

An optical disdrometer (OTT HydroMet, Parsivel^2) is used to measure the size distribution of the droplets, their velocity 1 m above the ground, and their kinetic energy (KE). This instrument measures the number of raindrops that pass through a sampling volume (generated by a 780 nm laser beam) with a size of approximately 3×18 cm^2 and an average thickness of 1 mm. The Parsivel^2 can detect particles as small as 0.2 mm in diameter and rain intensities as small as 0.001 mm/h. Detected particles are sorted into 32 diameter and 32 velocity classes [38].

2.1.2. Rain Module and Water Recirculation System

The droplet generators consist of 25-gauge hypodermic needles 25 mm long to ensure good droplet size and flow-rate control (see Figure 1d). A Luer-lock holder prevents unintentional needle removal. The rain module consists of 141 PP-R pipes (20 mm diameter, 3 mm wall thickness) arranged in three rows with a vertical spacing of 50 mm and a horizontal spacing of 75 mm (see Figure 1c). A horizontal shift of 25 mm between each row avoids overlap. Each pipe was drilled and threaded to install 121 needles with 25 mm spacing, obtaining a density of 1600 needles/m^2 and a total of about 17.000 droplet generators. The lower row is equipped with 4 mm diameter hollow caps to ensure the generation of large-diameter droplets (see Figure 1d). A layer of Teflon between each needle holder and its threaded hole ensures that the system is hydraulically sealed and prevents leakage. Two symmetrical manifolds, 0.2 m $\times$ 0.1 m $\times$ 3.5 m in size and made of AISI304 stainless steel, connect the ends of the pipes, creating a closed mesh network, ensuring rapid system response to water-head variations (see Figure 1a). In each manifold, 3 pressure sensors monitor the pressure in the rain module in real time. Two 1" flexible tubes connect the upstream manifold to the load tank, and two 5-micron mesh filters prevent impurities from reaching the rain module and clogging the needles. Air in the system is eliminated via two relief valves during filling operations, exploiting the fact that only the upstream manifold is connected to the reservoir and is slightly lower (in elevation) than the downstream manifold.

Rain is collected in nine collection tanks to ensure rapid runoff (see Figure 1a). A drainage system allows the volume of water in each sub-area to be sampled during tests. The drained water is conveyed to a collection tank where a submersible pump with a float switch pumps it to the ground tank, ensuring complete recirculation. An in-line 5 μm filter mesh filters the water, ensuring that there are no impurities in the recirculating water. The water employed in the experiments was ultrafiltered water treated with a Milli-Q system. A desktop PC running LabView connected to a National Instruments c-RIO device allows the monitoring and control of the entire experimental setup.

2.1.3. Redistribution Screen

A movable frame installed on four pulleys allows the positioning of different redistribution screens below the rain module. The nets can be strained to the target tension and replaced rapidly thanks to a pressure-sliding fastening system. Following Regmi and Thompson [25], only a 5 mm mesh (with 1 mm thick HDPE wires) was tested for different suspension distances in this study. A 4 mm mesh span guaranteed the breakage of almost all the large drops produced by the lowest drip plane. Furthermore, with a void index of 0.8, the mesh can intercept many droplets produced by the dripping upper planes while still allowing some of them to pass through. Thus, the redistribution of the diameters occurs homogeneously across the spectrum between 0 and 4.5 mm.

2.2. Preliminary Tests

2.2.1. Temperature-Independent Variables

Preliminary experiments were conducted to verify the theoretical relationship between the flow rate (Q) and water head (h) in the needles for different droplet formers. Since the flow within the needles is laminar under all the expected water-head conditions (0–50 cm), the flow rate can be described by the Hagen–Poiseuille equation for laminar flows, i.e.:

$$Q = \frac{\rho g h S^2}{8\pi\mu L},\qquad(1)$$

where ρ and μ are the water density and dynamic viscosity, respectively, and S and L are the needle cross-section and length, respectively. Rearranging (1), a temperature-independent flow rate Q^* can be defined as:

$$Q^* = Q\cdot\frac{\mu}{\rho} = \frac{g h S^2}{8\pi L}.\qquad(2)$$

By dividing the new flow rate by the needle-spacing area (A_{ns}), a temperature-independent rain rate (i^*) is obtained, i.e.:

$$i^* = \frac{Q^*}{A_{ns}}\qquad(3)$$

These novel parameters were employed to compare the results of tests conducted at different temperatures.

2.2.2. Experimental Setup

Preliminary tests involved volumetric measurement and imaging methods for greater reliability. A representation of the experimental setup inspired by the one described by Fernández-Raga et al. [39] is shown in Figure 2a. Drops produced by a single needle connected to a constant-load reservoir were collected and weighed, and water and room temperature were monitored throughout the tests. Each test lasted 30 min to ensure that a representative water volume was analysed. The temperature-independent needle flow rate was derived by dividing the volume collected during the trial and multiplying it by the viscosity of the water.

As for the volumetric method, a microphone was used to record the number of droplets. The mean droplet volume and diameter were obtained by dividing the collected volume by the number of fallen drops. As for the imaging method, a Nikon D800 camera with a Zeiss 50 mm MACRO lens was used to capture droplet images with a resolution of 50 px/mm using the shadowgraph technique and a shutter speed of 1/8000 s for better droplet edge detection. Droplet velocity, shape, diameter, and eccentricity near the ground were also determined using the shadowgraph technique and a Photron Nova S16 high-speed camera with a Nikkor 200 mm MACRO lens placed 30 cm above the ground. (An acoustic trigger allowed only in-focus droplets to be captured).

2.2.3. Results

Figure 2b shows the needle flow rate, Q^*, as a function of the water head. Such a relationship can be used to determine the intensity rate per Equation (3). The volumetric measurements agreed very well with the theoretical formula in Equation (2). Indeed, a significant increase in flow rate was observed by increasing the needle diameter. The rainfall intensities commonly reported in the literature vary depending on the case study. In stormwater studies, intensities range from 4.5 mm/h to more than 180 mm/h [40], while in erosion and chemical-transfer analyses, they are between 32 mm/h and 134 mm/h [41]. The 25-gauge needle provides an adequate flow range under the design conditions described here, providing intensities between 2 and 100 mm/h, with a mean droplet size of 2.43 mm.
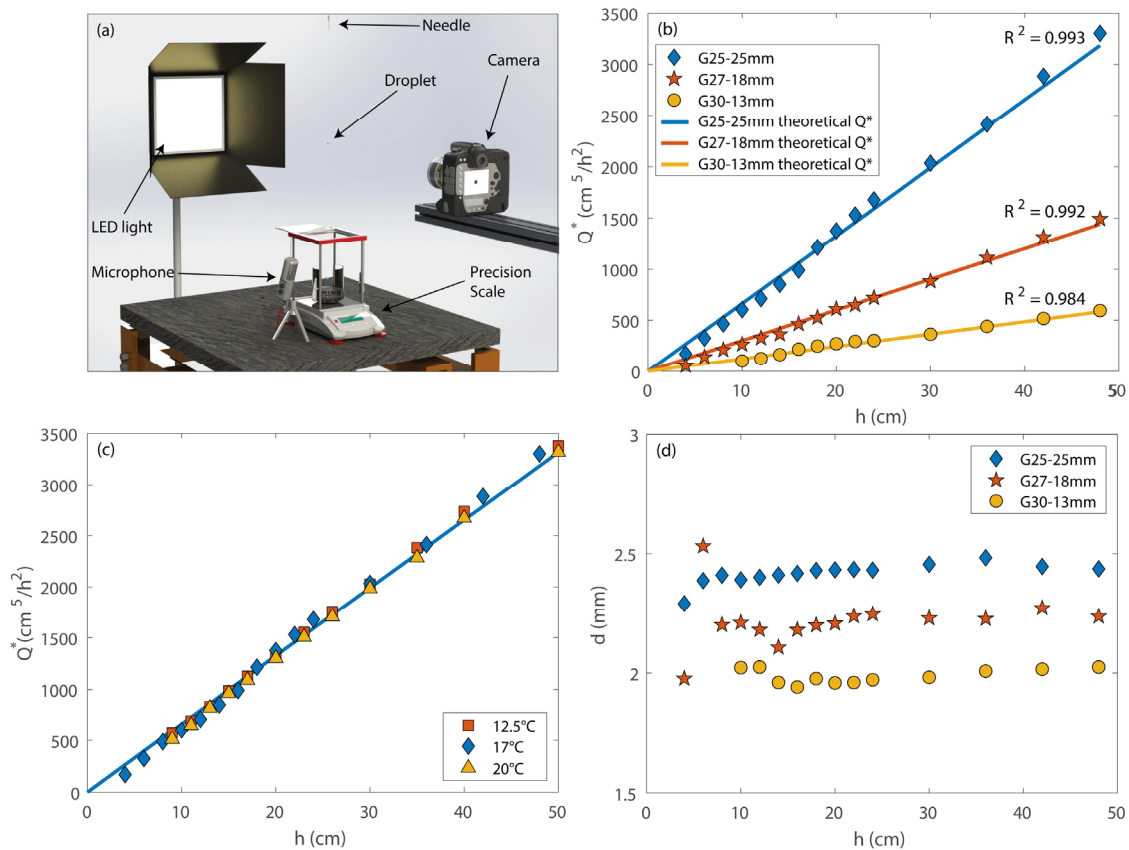
Figure 2. Results of the preliminary experiments conducted with different types of commercial hypodermic needles: (**a**) 3D rendering of the single-needle experimental setup; (**b**) one-needle flow rate, where the solid line denotes the theoretical Q* and the markers indicate the measured data; (**c**) 25-gauge needle flow rate for different water temperatures, where the solid line denotes the theoretical Q*; and (**d**) mean droplet diameters obtained from volumetric measurements.

Figure 2c shows the results of volumetric tests conducted with the 25-gauge needle for different temperatures. As can be seen, the outcomes agreed very well with the predicted flow rates when using Equation (2). The relationship between the mean drop diameter and the water head is shown in Figure 2d. The results highlighted that droplet diameter increases as needle size increases, though it is not affected by the water head. These outcomes were confirmed by the imaging measurements conducted with the 25-gauge needle. The results of the imaging method are summarised in Table 1. Note that only tests with 15 in-focus droplets or more were considered. As shown in the table, the diameters obtained via the two methods are almost identical, with differences of less than 2%.

Table 1. Comparison of mean diameters obtained by the volumetric method (d_v) and the imaging method (d_i) with the 25-gauge needle for a range of water heads. The absolute differences (Δ) between the two methods are also reported.

h (cm)	d_v (mm)	d_i (mm)	Δ (mm)
10	2.39	2.39	0
16	2.42	2.40	0.02
22	2.43	2.41	0.02
30	2.45	2.43	0.02
36	2.48	2.44	0.04
42	2.45	2.44	0.01
48	2.44	2.44	0

In addition to the previous tests, to generate droplets with diameters larger than 2.5 mm, some 25-gauge needles were equipped with 4 mm perforated caps. As shown in Table 2, this coupling allows the formation of larger droplets without compromising the system's flow rate, as the needle continues to act as a flow regulator.

Table 2. Single-needle analysis of the cap effect on simulated rain.

Head (cm)	Q* (cm^5/h^2)		d$_v$ (mm)	
	25 g	25 g + cap	25 g	25 g + cap
20	1137.7	1064.5	2.43	4.82
24	1326.4	1320	2.43	4.81
30	1572.8	1580.1	2.45	4.79
42	2136.7	2080	2.45	4.82

As for the drop velocity measurements, 14 videos with a resolution of 35 px/mm were analysed, and the results are shown in Figure 3. Although the mean droplet velocity was 7.47 m/s, which is 99% of the terminal velocity of a 2.5 mm drop [37], the mean diameter was 2.52 mm, which is slightly larger than the values obtained via the volumetric and imaging methods. This may be due to the lower resolution of the images and the technical difficulties in obtaining perfectly sharp edges with a 1 mm thick focus plane. Figure 3a shows a few frames of a droplet falling with a velocity close to the terminal velocity. Droplets showed a slightly enlarged shape at the bottom caused by the drag force producing a mean eccentricity of 0.119, in agreement with the values reported in the literature [42].
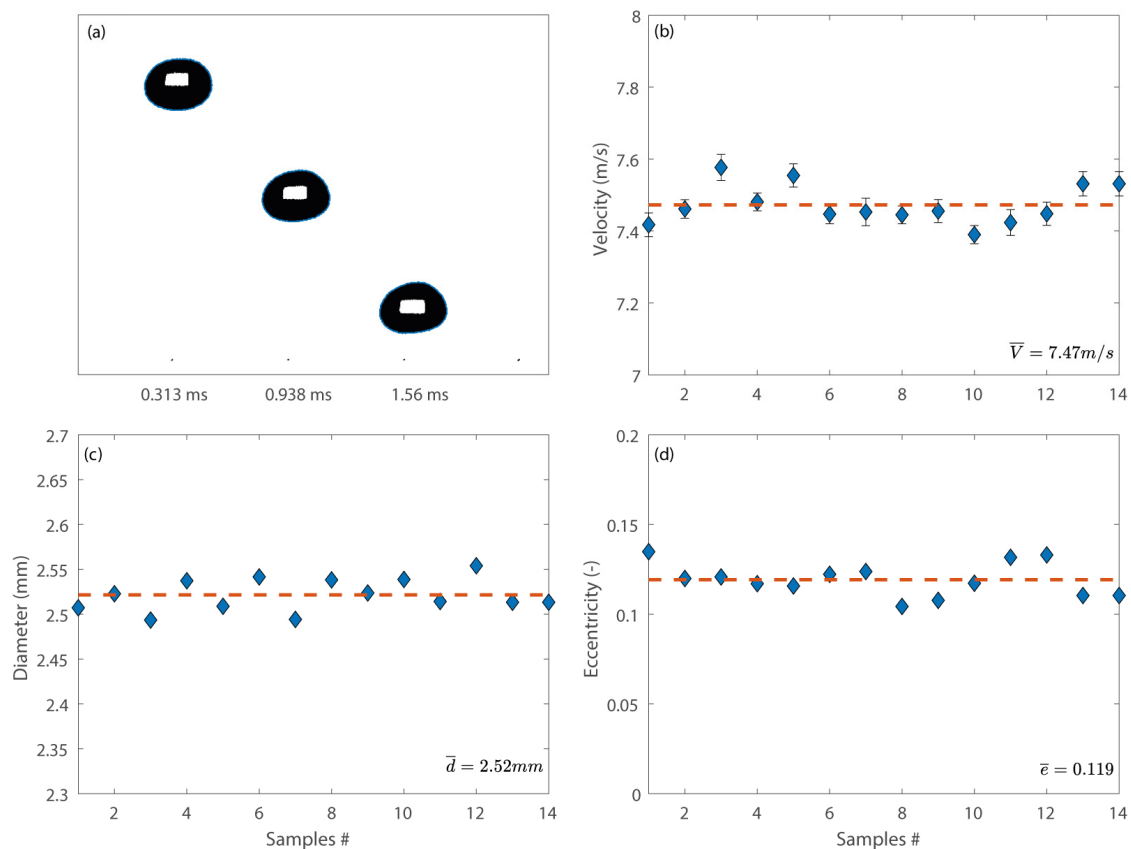

Figure 3. Results of high-speed camera analysis: (**a**) a few frames of a falling drop captured by the high-speed camera, with the contours identified by the analysis also shown; (**b**) mean droplet velocity; (**c**) mean droplet diameter; and (**d**) mean droplet eccentricity.

2.3. Calibration Procedure

At the beginning of each test, the rain module was empty, and the motorised valves closed. During the loading phase, the pump was turned on, the valves were opened, and the rain module was gradually filled by increasing the level in the loading tank until the air was eliminated. Successively, the spillway was lowered to the desired level. Following a decreasing load curve for the planned experiments, drip-plane start-up transients were avoided by minimising the time between experiments, starting from the maximum level and gradually proceeding downward. Pressure sensors monitored the steady-state conditions in the rain module. The flow rate on the ground generated by the system, the mean intensity, the spatial variation, and the reproducibility rate were assessed via volumetric measurements of the nine collection tanks. The ground measurements had different durations depending on the simulated intensity to ensure that the same volume was always collected. Water temperatures were monitored during each test to determine water viscosity. Once a measurement was completed, the spillway level was lowered to the desired elevation, and the following measures were started only after the new steady-state conditions were achieved. Once all the experiments were completed, the pump was turned off, and the rain module was emptied by lowering the level in the load tank below the collector height.

Since the tests were conducted before the installation of the water recirculation system, the water heads were limited to 24 cm to reduce water consumption, ensuring that all the experiments could be carried out. Rain intensities obtained from the volumetric measurements were then used to evaluate the Christiansen uniformity coefficient (UC) defined in Equation (4), where x_i is the i-th measured datum, n is the number of measurements, and $\bar{x}$ is the measurements' average value, i.e.:

$$\text{UC} = 100 \left(1 - \frac{\sum_1^n |x_i - \bar{x}|}{n \cdot \bar{x}} \right). \tag{4}$$

Following the same procedure described for the intensity calibration, droplet size distribution tests were conducted for seven different configurations: one with no redistribution screen and six with the grid at increasing distances from the drip plane (D1–D6). The water-head conditions could be accurately replicated for each configuration by controlling the spillway position, ensuring 15 min of steady-state conditions for each test. During the experiments, the disdrometer performed measurements with a sampling frequency of 60 s. Following the *Manual of Surface Weather Observation Standards* [43], the collected data were divided into four intensity classes, and a representative droplet size distribution (DSD) was obtained for each category. Since the tests were conducted by limiting the maximum water head, only three of the four classes listed in Table 3 were simulated during these experiments.

Table 3. Rain intensity classification according to the MSWOS.

Classification	Intensity (mm/h)
Light	<2.5
Moderate	2.6–7.5
Heavy	7.6–50
Torrential	>50

A second Parsivel^2 disdrometer was installed on the roof of the Hydraulics Laboratory at the Polytechnic of Turin in July 2020; since then, it has been collecting data with a sampling rate of 60 s. These data were used as reference values for the rain generated in the rainfall simulator rather than employing rainfall data from the literature [44–46], which show large variability.

3. Results

3.1. Properties of Simulated Rain

3.1.1. Rain without a Redistribution Grid

Figure 4b shows the application-rate curve of the system for the relationship between intensity and water head (note that Figure 4a displays the elevation of the three dip planes, on which the relationships in Figure 4b depend). Based on the results of the preliminary tests (see Section 2.1.3), the expected application curves for each drip plane (p_i) were defined using Equation (3) and by dividing each contribution by the number of planes. As shown in Equation (5), the expected relationship can be described as the sum of the contributions from each drip plane. Once the water reaches the activation level of one of the planes, dripping starts, increasing the flow rate on the ground (see the coloured lines in Figure 4b) and leading to a discontinuous trend.

$$\begin{cases} i^* = p_1 & 5\,\text{cm} \leq h < 10\,\text{cm} \\ i^* = p_1 + p_2 & 10\,\text{cm} \leq h < 15\,\text{cm} \\ i^* = p_1 + p_2 + p_3 & 15\,\text{cm} \leq h \end{cases} \tag{5}$$
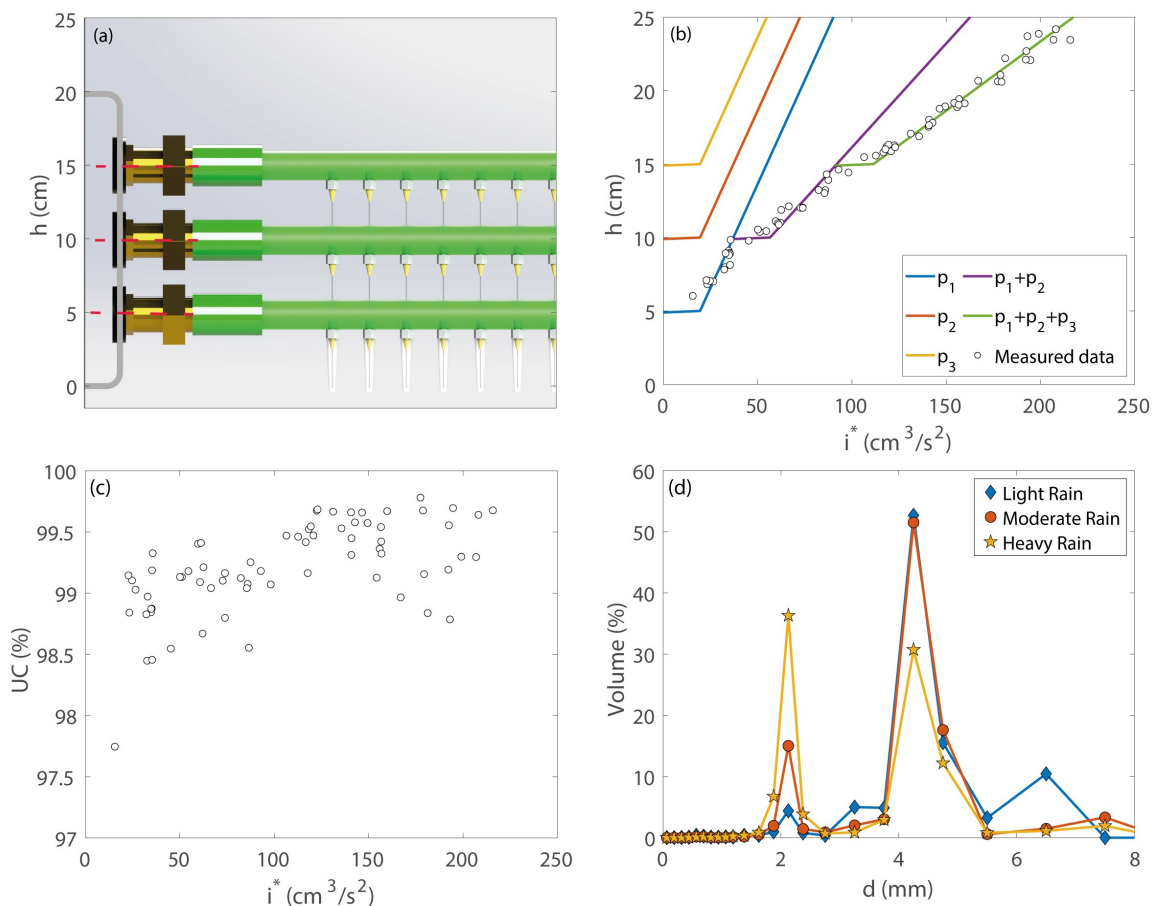

Figure 4. Results of rainfall intensity simulations: (**a**) side view of the rain module with elevations of individual drip planes; (**b**) temperature-independent rain rate as a function of the water head from theory and measured data, where p_1, p_2, and p_3 are the application-rate curves for the bottom, middle, and top dripping planes, respectively; (**c**) Christiansen uniformity coefficients as a function of the temperature-independent rain rate; and (**d**) droplet size distribution produced by the rain module for the three intensity classes used in the experiments.

In contrast, the measured intensity (see the empty circles in Figure 4b) shows a continuous trend which is likely due to potential geometrical imperfections in the drip

system, friction losses, and surface tension forces that play a crucial role when the water head on a drip plane is low.

The Christiansen uniformity coefficient was defined for each test based on the volumes collected in each of the nine collection tanks, as described in Equation (4). According to the classification of the American Society of Agricultural Engineers [47] (see Table 4), the simulated rain had excellent spatial uniformity, with UCs ranging between 97.7% and 99.5% and which grew as the intensity increased (see Figure 4c). These results show the high spatial uniformity of the simulated rainfall, which ensured similar simulated conditions over the entire test area.

Table 4. Rain-rate intensity classification according to ASAE.

Classification	UC (%)
Excellent	>90
Good	80–90
Fair	70–80
Poor	60–70
Unacceptable	<60

Figure 4d shows the droplet size distributions produced by the rain module as acquired by the disdrometer. The measurements showed two characteristic diameters that well defined the simulated rainfall distribution. These diameters corresponded to those produced by the two droplet formers used in the setup (see Section 2.1.3). A change in the volume distribution between the two diameters became evident as the rain intensity increased. This phenomenon was due to the subsequent activation of the upper drip planes: with light rain, only the lower plane equipped with the perforated caps dripped; as the intensity increased, the upper planes were activated, producing smaller droplets. The results for this configuration are also summarised in the first row of Table 5, where the mass median diameter (D_{50}) of droplets is reported as a representative value of the DSD.

Table 5. Main properties of simulated rain for all configurations tested: D_{50} indicates the median mass diameter and $\overline{KE}$ the mean kinetic energy of the droplets.

Test ID	Grid Distance from the Rain Module (cm)	D_{50} LR [1] (mm)	D_{50} MR [2] (mm)	D_{50} HR [3] (mm)	$\overline{KE}$ LR [1] (J/m^2 h^{-1})	$\overline{KE}$ MR [2] (J/m^2 h^{-1})	$\overline{KE}$ HR [3] (J/m^2 h^{-1})
NG [4]	-	4.05	4.00	3.13	63.9	163.2	1594.9
D1	25	1.95	2.17	1.94	40.3	109.4	538.2
D2	50	2.13	2.16	1.86	50.2	107.5	536.3
D3	100	1.40	1.64	1.63	31.2	87.7	399.6
D4	200	1.15	1.27	1.22	24.7	71.3	271.4
D5	300	1.08	1.11	1.10	21.0	56.7	228.8
D6	400	1.01	1.02	1.03	20.2	51.0	202.5

Notes: [1] LR—light rain. [2] MR—moderate rain. [3] HR—heavy rain. [4] NG—no grid.

3.1.2. Rain with the Redistribution Screen

This section investigates the effects of the redistribution screen on the droplet size distribution. Table 5 summarises the main results obtained for the six configurations tested plus the configuration with no grid. With the redistribution screen, the mass median rain diameter varied with rain intensity, showing a local maximum for moderate intensity. However, as the screen was moved further from the rain module and closer to the ground, this maximum was reduced, and the median mass diameter became independent of rain intensity. Moving the screen closer to the ground led to a decrease in the median mass

diameter and the rainfall kinetic energy. In more detail, both D_{50} and mean KE values were reduced by 50% with configurations D1 to D6.

Figure 5 shows the droplet size distribution generated with the redistribution screen at selected distances from the rain module and for all rain intensities (note that four out of six configurations are shown to ease visualisation). The results show that increasing the distance from the drip plane significantly reduced the percentage of drops with a diameter greater than 2 mm. However, compared to the light rain intensity scenario, there was an increase in drops with diameters greater than 2.5 mm for moderate- and heavy-rain scenarios. An explanation of these results can be found in the drip plane's geometry and the redistribution grid's characteristics. Only the lower drip plane is active for intensities in the range of 0–10 mm/h (which corresponds to light and moderate rain). As the intensity increases, water accumulation occurs on the surface of the grid, resulting in significant drops detaching. For intensities exceeding 10 mm/h (corresponding to heavy rain), the activation of the upper planes produces smaller droplets. At the same time, increasing the overall kinetic energy on the redistribution screen, that is, increasing the distance between the grid and rain module, reduces the accumulation and detachment of large droplets.
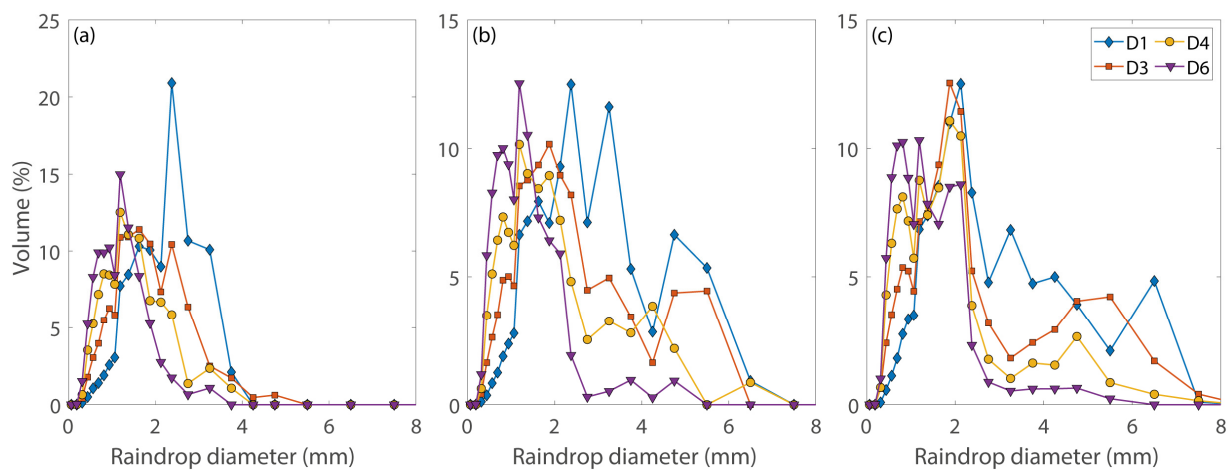

Figure 5. Droplet size distributions were produced with a redistribution screen for all intensity classes used in the experiments: (**a**) light rain; (**b**) moderate rain; and (**c**) heavy rain.

Droplet size and velocity distributions for the different rain intensity classes are shown in the simulated rainfall spectra in Figure 6. These plots represent the percentages of raindrops falling in 60 s sorted by diameter and velocity classes. The results obtained with the configurations that best approximated the natural droplet size distributions for each of the three intensity classes analysed are shown. The terminal-speed curve as a function of rainfall diameter [25] is also shown for reference. The results confirm that the elevation of the drip plane allows the terminal velocity to be correctly simulated for the entire rainfall spectrum.

3.2. Natural Rain

The properties of the local-scale rain data recorded by the disdrometer installed on the roof of the Hydraulics Laboratory are presented here; they are to be used as a benchmark for the rain events produced with the rainfall simulator. Since its installation, the disdrometer has collected more than 45,000 measurements. The dataset was filtered to remove low-quality/erroneous data, and observations with intensities lower than 0.1 mm/h or fewer than ten particles were detected. Following Jaffrain et al. [48], a validation procedure removed any outliers by filtering out particles that did not satisfy the following condition:

$$|V(d)_{\text{measured}} - V(d)_{\text{Gunn}}| \leq 0.6\, V(d)_{\text{Gunn}} \tag{6}$$

where $V(d)_{measured}$ is the droplet velocity measured by the disdrometer and $V(d)_{Gunn}$ is the theoretical terminal velocity, according to Gunn et al. [37].

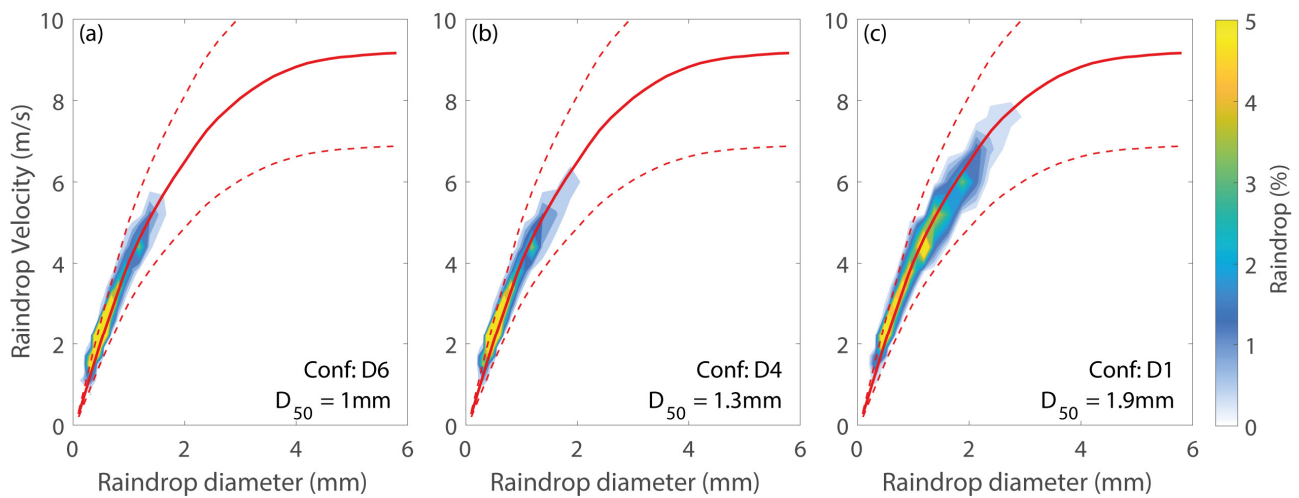**Figure 6.** Simulated rainfall spectra for each rain intensity class: (**a**) light rain; (**b**) moderate rain; and (**c**) heavy rain. The solid lines denote Gunn–Kinzer terminal-velocity curves, and the dashed lines indicate the lower and upper confidence bounds, defined as ±25% of the terminal velocity. The configuration with the best approximation of natural conditions for each intensity class is shown in the figure. The D_{50} values for the designs are also shown.

Figure 7a displays the relationship between the median droplet diameter and the rain intensities. The median raindrop diameter increased with the rain intensity, ranging between 0.8 and 2.5 mm for intensities in the range of 0–60 mm/h (which includes all the intensity classes analysed). In agreement with what has been found in the literature [30,49–53], an empirical formulation ($D_{50} = aI^p$) that fits the local data is proposed. The values of the parameters a and p obtained here fall within the ranges described in the literature. The different parameterisations and values of the parameters a and p that have been proposed in previous works were due to the significant variability in the meteorological contexts the authors considered. The relationship between kinetic energy and rain intensity is shown in Figure 7b, together with the best-fit power function. As for the median mass diameter, the identified power-law parameters fall within the ranges described in the literature [54,55].
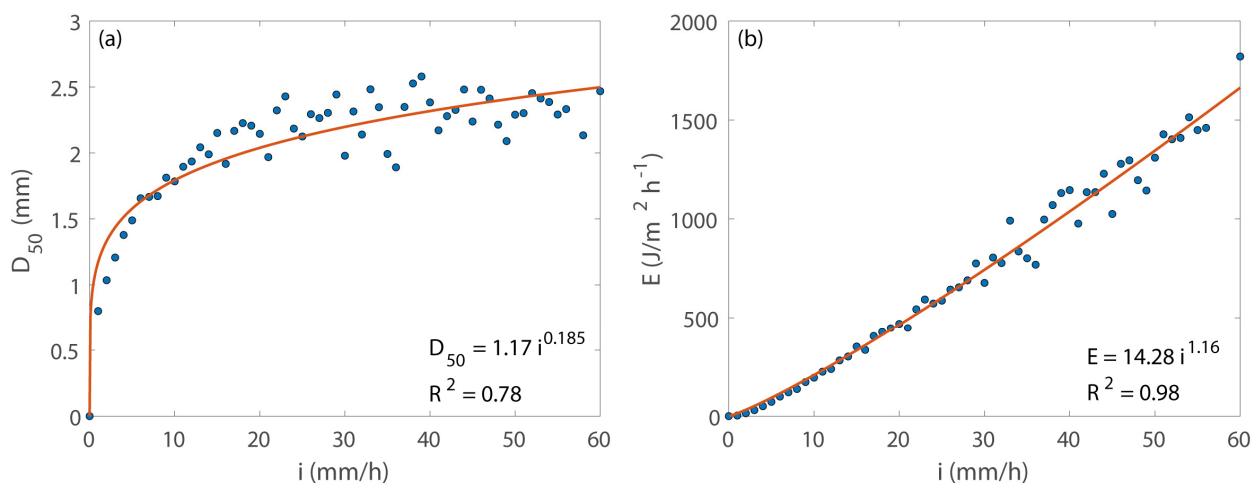

Figure 7. Properties of natural local-scale rain. Droplet mass median diameter (**a**) and kinetic energy (**b**) versus rain intensity. Solid lines represent the power functions that best fit the experimental data. Their equations are reported together with R^2 values.

Droplet size and velocity distributions for the three rainfall intensity classes are shown in Figure 8. As expected, the distributions show an increase in particle size as the intensity increases, which is confirmed by the median mass diameter reported for each class analysed.
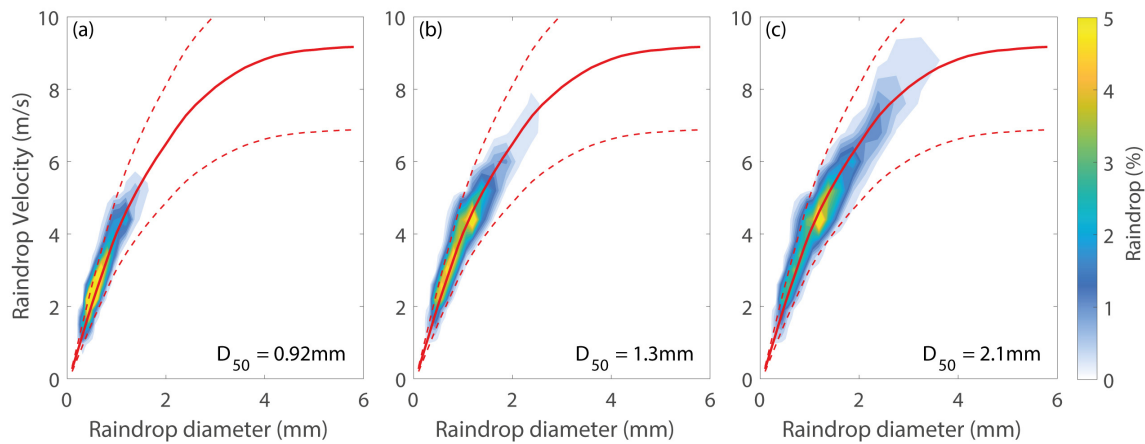

Figure 8. Natural rainfall spectra for each rain intensity class: (**a**) light rain; (**b**) moderate rain; and (**c**) heavy rain. The solid lines denote Gunn–Kinzer terminal-velocity curves, and the dashed lines indicate the lower and upper confidence bounds, defined as ±25% of the terminal velocity. The mass median drop diameter for each rain intensity class is also shown.

3.3. Comparing Natural and Simulated Rain Properties

The spatial uniformity results presented in Section 3.1.1 show values ranging between 97% and 99%, which are even higher than those reported in the literature for natural rainfall [40]. A comparison of the droplet size distribution of natural rain and its best approximation among the configurations tested with the simulator is presented in Figure 9a–c. The results highlight that the droplet size distribution generated by the redistribution screen employed is satisfactory. Although there are some discrepancies, the distributions show similar trends, as evidenced by the D_{50} values identified.

The rain simulator can generate rainfall with a kinetic energy–intensity relationship that is consistent with natural rainfall up to an intensity of 30 mm/h (see Figure 9d). Above this intensity, the effects of the redistribution screen are noticeable, as it limits the number of large drops that can reach the ground. Tests have confirmed this result with no screen in place, where the kinetic energy was always higher than for the natural rainfall and any other configuration. In natural phenomena, as the intensity increases, so does the number of large drops [30,51]. In contrast, in our setup, we were limited by the mesh size of the redistribution screen. Nevertheless, the droplet size and velocity distributions provided comparable results (see Figures 6–8), attesting to the simulator's ability to achieve the terminal velocity for all diameter classes.
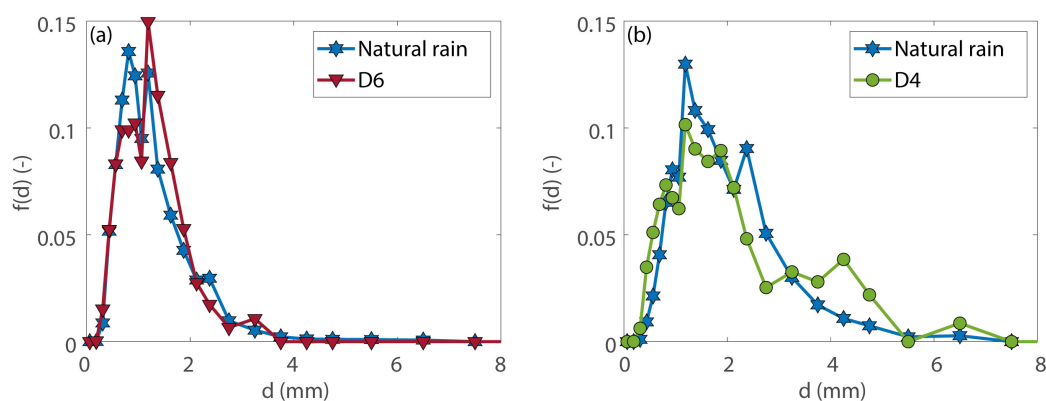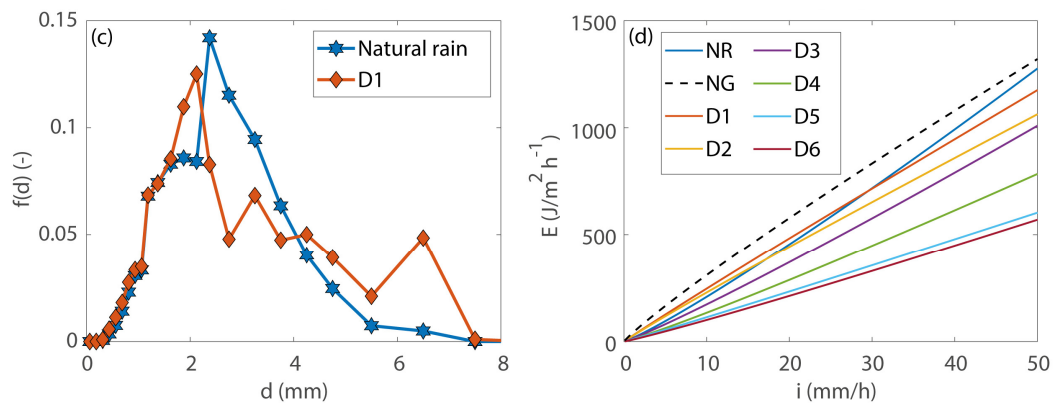

Figure 9. *Cont.*

Figure 9. Natural (NR) and simulated rainfall property comparisons. Droplet size distributions comparing natural rain with a selected configuration of the simulator: (**a**) DSD for light rain; (**b**) DSD for moderate rain; and (**c**) DSD for heavy rain. (**d**) Best-fit power functions of kinetic energy versus intensity for natural rain and all simulator configurations.

4. Discussion

Spatial uniformity and the simulation of kinetic energy levels and droplet size distributions that resemble those of natural rain are essential elements in the development of a rainfall simulator. The apparatus presented in this study showed high spatial homogeneity over the entire intensity range analysed. Thanks to the recirculation system of the precipitated water, the system can operate continuously without interruptions, making it possible to simulate long-lasting phenomena. The water-level control system in the load tank presented in this study also guarantees high temporal homogeneity by allowing a constant water head to be maintained for a desired length of time. The presence of specially selected needle formers in the setup coupled with the water-level control system in the reservoir provides a significant advantage in terms of intensity control over other existing systems [4,56,57], allowing a wide range of intensities to be generated with 0.3 mm/h increments. In addition, the water-level control system allows the acting water head over the system to be changed easily, allowing for the production of complex events that follow recorded patterns.

To our knowledge, the simulator size presented in this study is among the largest in the literature. Other setups offer larger simulation surfaces [6,36,57] or higher fall heights [25], but none present these two characteristics simultaneously, making this system a unique research tool. Regarding kinetic energy, the simulator can faithfully reproduce rainfall with intensities of up to 30 mm/h, guaranteeing a correct kinetic energy–intensity relationship. However, above this intensity, the presence of the redistribution screen limits the number of large drops available. Nevertheless, this discrepancy does not represent a limitation, as it is still possible to simulate the effects of intensities above the indicated limit simply by increasing the simulated intensity to achieve the desired kinetic energy values. Furthermore, using optical disdrometers to measure the droplet size distribution rather than manual systems (e.g., flour pellets) ensures the accurate comparison of the data obtained for simulated and natural rainfall, hence allowing for precise calibration of the simulator.

5. Conclusions

This study has presented the design and fine-tuning of a large-scale, indoor, needle-type rainfall simulator that can accurately simulate the properties of natural rain. The proposed system consists of a redistribution screen suspended below a rain module at the top of a 3.5 × 4 × 10.4 m³ tower which is fed by a loading tank with motorised level regulation. A precise calibration of the experimental setup was carried out using local natural rainfall data collected in a 30-month measurement campaign. Furthermore, different distances of the screen from the rain module were investigated to identify the

configurations that best replicate natural conditions for three rain intensity classes in terms of simulated intensity, kinetic energy, and spatial/temporal homogeneity. The results presented in this study show that the developed rainfall simulator represents a unique and versatile research tool due to its key features, which can be summarised as follows:

- A wide range of rain intensities that can be varied in 0.3 mm/h increments;
- Different droplet formers consisting of hypodermic needles (25-gauge) and hypodermic needles coupled with perforated caps can produce 2.4 mm and 4.5 mm diameter droplets while maintaining the same effluent flow rate;
- The high density of droplet formers ensures the high spatial uniformity of simulated rain over the entire intensity range, covering an area of 14 m^2;
- Good reproduction of the droplet size distribution of natural rainfall can be achieved by varying the elevation of the redistribution screen depending on the rain intensity;
- The achievement of terminal velocity for all classes of diameter, ensuring the accurate reproduction of rainfall kinetic energy;
- Due to its unique characteristics, this system can be used to investigate soil erosion, runoff and urban washoff phenomena on a large scale in great detail. In addition, the possibility of simulating rain with high temporal homogeneity over long periods creates opportunities for numerous applications in the accelerated study of the chemical and physical effects of rain on the properties of soils, pavements, materials, and surfaces.

Author Contributions: Conceptualization, D.P. and R.B.; methodology, R.B.; software, R.B.; validation, R.B.; investigation, R.B. and A.C.; data curation, R.B.; resources, R.B. and A.C.; writing—original draft preparation, R.B.; writing—review and editing, D.P.; supervision, D.P. and A.C. All authors have read and agreed to the published version of the manuscript.

Data Availability Statement: The data presented in this study are available on request from the corresponding author.

Conflicts of Interest: The authors declare no conflict of interest.

References

1. Bhowmick, T.; Iovieno, M. Direct Numerical Simulation of a Warm Cloud Top Model Interface: Impact of the Transient Mixing on Different Droplet Population. *Fluids* **2019**, *4*, 144. [CrossRef]
2. Götzfried, P.; Kumar, B.; Shaw, R.A.; Schumacher, J. Droplet Dynamics and Fine-Scale Structure in a Shearless Turbulent Mixing Layer with Phase Changes. *J. Fluid Mech.* **2017**, *814*, 452–483. [CrossRef]
3. de Lozar, A.; Mellado, J.P. Cloud Droplets in a Bulk Formulation and Its Application to Buoyancy Reversal Instability. *Q. J. R. Meteorol. Soc.* **2014**, *140*, 1493–1504. [CrossRef]
4. Lassu, T.; Seeger, M.; Peters, P.; Keesstra, S.D. The Wageningen Rainfall Simulator: Set-up and Calibration of an Indoor Nozzle-Type Rainfall Simulator for Soil Erosion Studies. *Land Degrad. Dev.* **2015**, *26*, 604–612. [CrossRef]
5. Nassif, S.H. Hydrological Studies of a Laboratory Catchment Area under Rainfall Simulation. Ph.D. Thesis, University of Salford, Manchester, UK, 1973.
6. Kim, H.; Ko, T.; Jeong, H.; Ye, S. The Development of a Methodology for Calibrating a Large-Scale Laboratory Rainfall Simulator. *Atmosphere* **2018**, *9*, 427. [CrossRef]
7. Clarke, M.A.; Walsh, R.P.D. A Portable Rainfall Simulator for Field Assessment of Splash and Slopewash in Remote Locations. *Earth Surf. Process. Landf.* **2007**, *32*, 2052–2069. [CrossRef]
8. Nearing, M.A.; Bradford, J.M.; Holtz, R.D. Measurement of Force vs. Time Relations for Waterdrop Impact. *Time Relations for Waterdrop Impact. Soil Sci. Soc. Am. J.* **1986**, *50*, 1532–1536. [CrossRef]
9. Mermut, A.R.; Luk, S.H.; Römkens, M.J.M.; Poesen, J.W.A. Soil Loss by Splash and Wash during Rainfall from Two Loess Soils. *Geoderma* **1997**, *75*, 203–214. [CrossRef]
10. Sharma, P.P.; Gupta, S.C.; Rawls, W.J. Soil Detachment by Single Raindrops of Varying Kinetic Energy. *Soil Sci. Soc. Am. J.* **1991**, *55*, 301–307. [CrossRef]

11. Battany, M.C.; Grismer, M.E. Development of a Portable Field Rainfall Simulator for Use in Hillside Vineyard Runoff and Erosion Studies. *Hydrol. Process.* **2000**, *14*, 1119–1129. [CrossRef]

12. Meyer, L.D.; Harmon, W.C. Multiple-Intensity Rainfall Simulator for Erosion Research on Row Sideslopes. *Trans. ASAE* **1979**, *22*, 0100–0103. [CrossRef]

13. Fernández-Raga, M.; Campo, J.; Rodrigo-Comino, J.; Keesstra, S.D. Comparative Analysis of Splash Erosion Devices for Rainfall Simulation Experiments: A Laboratory Study. *Water* **2019**, *11*, 1228. [CrossRef]

14. Aksoy, H.; Unal, N.E.; Cokgor, S.; Gedikli, A.; Yoon, J.; Koca, K.; Inci, S.B.; Eris, E. A Rainfall Simulator for Laboratory-Scale Assessment of Rainfall-Runoff-Sediment Transport Processes over a Two-Dimensional Flume. *CATENA* **2012**, *98*, 63–72. [CrossRef]

15. Abudi, I.; Carmi, G.; Berliner, P. Rainfall Simulator for Field Runoff Studies. *J. Hydrol.* **2012**, *454–455*, 76–81. [CrossRef]

16. Boulange, J.; Malhat, F.; Jaikaew, P.; Nanko, K.; Watanabe, H. Portable Rainfall Simulator for Plot-Scale Investigation of Rainfall-Runoff, and Transport of Sediment and Pollutants. *Int. J. Sediment Res.* **2019**, *34*, 38–47. [CrossRef]

17. Naves, J.; Anta, J.; Suárez, J.; Puertas, J. Hydraulic, Wash-off and Sediment Transport Experiments in a Full-Scale Urban Drainage Physical Model. *Sci. Data* **2020**, *7*, 44. [CrossRef] [PubMed]

18. Silburn, D.M. Characterising Pesticide Runoff from Soil on Cotton Farms Using a Rainfall Simulator. Ph.D Thesis, University of Sydney, Sydney, NSW, Australia, 2003.

19. Zhang, X.C.; Norton, D.; Nearing, M.A. Chemical Transfer from Soil Solution to Surface Runoff. *Water Resources Research.* **1997**, *33*, 809–815. [CrossRef]

20. Stašek, J.; Krása, J.; Mistr, M.; Dostál, T.; Devátý, J.; Středa, T.; Mikulka, J. Using a Rainfall Simulator to Define the Effect of Soil Conservation Techniques on Soil Loss and Water Retention. *Land* **2023**, *12*, 431. [CrossRef]

21. Macák, M.; Galambošová, J.; Kumhála, F.; Barát, M.; Kroulík, M.; Šinka, K.; Novák, P.; Rataj, V.; Misiewicz, P.A. Reduction in Water Erosion and Soil Loss on Steep Land Managed by Controlled Traffic Farming. *Land* **2023**, *12*, 239. [CrossRef]

22. Alves, M.A.B.; de Souza, A.P.; de Almeida, F.T.; Hoshide, A.K.; Araújo, H.B.; da Silva, A.F.; de Carvalho, D.F. Effects of Land Use and Cropping on Soil Erosion in Agricultural Frontier Areas in the Cerrado-Amazon Ecotone, Brazil, Using a Rainfall Simulator Experiment. *Sustainability* **2023**, *15*, 4954. [CrossRef]

23. García-Haba, E.; Naves, J.; Hernández-Crespo, C.; Goya-Heredia, A.; Suárez, J.; Anta, J.; Andrés-Doménech, I. Influence of Sediment Characteristics on Long-Term Hydrology and Water Quality Behaviour during the Clogging Process of a Permeable Asphalt. *J. Water Process Eng.* **2023**, *53*, 103658. [CrossRef]

24. Rodríguez, I.; Ortiz, A.; Caldevilla, P.; Giganto, S.; Búrdalo, G.; Fernández-Raga, M. Comparison between the Effects of Normal Rain and Acid Rain on Calcareous Stones under Laboratory Simulation. *Hydrology* **2023**, *10*, 79. [CrossRef]

25. Regmi, T.P.; Thompson, A.L. RAINFALL SIMULATOR FOR LABORATORY STUDIES. *Appl. Eng. Agric.* **2000**, *16*, 641–647. [CrossRef]

26. Kavian, A.; Mohammadi, M.; Cerda, A.; Fallah, M.; Abdollahi, Z. Simulated Raindrop's Characteristic Measurements. A New Approach of Image Processing Tested under Laboratory Rainfall Simulation. *CATENA* **2018**, *167*, 190–197. [CrossRef]

27. Hignett, C.T.; Gusli, S.; Cass, A.; Besz, W. An Automated Laboratory Rainfall Simulation System with Controlled Rainfall Intensity, Raindrop Energy and Soil Drainage. *Soil Technol.* **1995**, *8*, 31–42. [CrossRef]

28. Rončević, V.; Živanović, N.; van Boxel, J.H.; Iserloh, T.; Štrbac, S. Dripping Rainfall Simulators for Soil Research—Performance Review. *Water* **2023**, *15*, 1314. [CrossRef]

29. Kohl, R.A. Drop Size Distribution from Medium-Sized Agricultural Sprinklers. *Trans. ASAE* **1974**, *17*, 690–0693. [CrossRef]

30. Laws, J.O.; Parsons, D.A. The Relation of Raindrop-Size to Intensity. *Trans. Am. Geophys. Union* **1943**, *24*, 452. [CrossRef]

31. Bryan, R.B.S. *Surface Crusts Formed under Simulated Rainfall on Canadian Soils*; Report to a conference held in Pisa; CNR: Pisa, Italy, 1973.

32. Bowyer-Bower, T.A.S.; Burt, T.P. Rainfall Simulators for Investigating Soil Response to Rainfall. *Soil Technol.* **1989**, *2*, 1–16. [CrossRef]

33. Swanson, N.P.; Dedrick, A.R. Soil Particles and Aggregates Transported in Water Runoff Under Various Slope Conditions Using Simulated Rainfall. Available online: https://elibrary.asabe.org/abstract.asp??JID=3&AID=39645&CID=t1967&v=10&i=2&T=1 (accessed on 17 September 2022).

34. Morin, J.; Goldberg, D.; Seginer, I. A Rainfall Simulator with a Rotating Disk. Available online: https://elibrary.asabe.org/abstract.asp??JID=3&AID=39599&CID=t1967&v=10&i=1&T=1 (accessed on 17 September 2022).

35. Chevone, B.I.; Yang, Y.S.; Winner, W.E.; Storks-Cotter, I.; Long, S.J. A Rainfall Simulator for Laboratory Use in Acidic Precipitation Studies. *J. Air Pollut. Control Assoc.* **1984**, *34*, 355–359. [CrossRef]

36. Chow, V.T.; Harbaugh, T.E. Raindrop Production for Laboratory Watershed Experimentation. *J. Geophys. Res.* **1965**, *70*, 6111–6119. [CrossRef]

37. Gunn, R.; Kinzer, G.D. The terminal velocity of fall for water droplets in stagnant air. *J. Atmos. Sci.* **1949**, *6*, 243–248. [CrossRef]

38. Tokay, A.; Wolff, D.B.; Petersen, W.A. Evaluation of the New Version of the Laser-Optical Disdrometer, OTT Parsivel2. *J. Atmos. Ocean. Technol.* **2014**, *31*, 1276–1288. [CrossRef]

39. Fernández-Raga, M.; Cabeza-Ortega, M.; González-Castro, V.; Peters, P.; Commelin, M.; Campo, J. The Use of High-Speed Cameras as a Tool for the Characterization of Raindrops in Splash Laboratory Studies. *Water* **2021**, *13*, 2851. [CrossRef]

40. Kathiravelu, G.; Lucke, T.; White, R.; Nichols, P.W. Review on Design Requirements of a Rainfall Simulator for Urban Stormwater Studies. In Proceedings of the 2014 Stormwater Queensland Conference, Townsville, QLD, Australia, 6 August 2014.

41. Ahuja, L.R. Modeling Soluble Chemical Transfer to Runoff with Rainfall Impact as a Diffusion Process. *Soil Sci. Soc. Am. J.* **1990**, *54*, 312–321. [CrossRef]
42. Beard, K.V.; Bringi, V.N.; Thurai, M. A New Understanding of Raindrop Shape. *Atmos. Res.* **2010**, *97*, 396–415. [CrossRef]
43. Environment and Climate Change Canada. *MANOBS—Manual of Surface Weather Observations*; Environment and Climate Change Canada: Gatineau, CA, USA, 2013.
44. Tokay, A.; D'Adderio, L.P.; Wolff, D.B.; Petersen, W.A. Development and Evaluation of the Raindrop Size Distribution Parameters for the NASA Global Precipitation Measurement Mission Ground Validation Program. *J. Atmos. Ocean. Technol.* **2020**, *37*, 115–128. [CrossRef]
45. Chen, B.; Hu, Z.; Liu, L.; Zhang, G. Raindrop Size Distribution Measurements at 4,500 m on the Tibetan Plateau During TIPEX-III. *J. Geophys. Res. Atmos.* **2017**, *122*, 106. [CrossRef]
46. Friedrich, K.; Kalina, E.A.; Aikins, J.; Steiner, M.; Gochis, D.; Kucera, P.A.; Ikeda, K.; Sun, J. Raindrop Size Distribution and Rain Characteristics during the 2013 Great Colorado Flood. *J. Hydrometeorol.* **2016**, *17*, 53–72. [CrossRef]
47. Christiansen, J.E. *Irrigation by Sprinkling*; Bulletin n. 670; University of California Agricultural Experiment Station: Berkeley, CA, USA, 1942.
48. Jaffrain, J.; Berne, A. Experimental Quantification of the Sampling Uncertainty Associated with Measurements from PARSIVEL Disdrometers. *J. Hydrometeorol.* **2011**, *12*, 352–370. [CrossRef]
49. Atlas, D. Optical Extinction by Rainfall. *J. Atmos. Sci.* **1953**, *10*, 486–488. [CrossRef]
50. Nanko, K.; Moskalski, S.M.; Torres, R. Rainfall Erosivity–Intensity Relationships for Normal Rainfall Events and a Tropical Cyclone on the US Southeast Coast. *J. Hydrol.* **2016**, *534*, 440–450. [CrossRef]
51. Best, A.C. The Size Distribution of Raindrops. *Q. J. R. Meteorol. Soc.* **1950**, *76*, 16–36. [CrossRef]
52. Brandt, C.J. The Size Distribution of Throughfall Drops under Vegetation Canopies. *CATENA* **1989**, *16*, 507–524. [CrossRef]
53. Willis, P.T. Functional Fits to Some Observed Drop Size Distributions and Parameterization of Rain. *J. Atmos. Sci.* **1984**, *41*, 1648–1661. [CrossRef]
54. Salles, C.; Poesen, J.; Sempere-Torres, D. Kinetic Energy of Rain and Its Functional Relationship with Intensity. *J. Hydrol.* **2002**, *257*, 256–270. [CrossRef]
55. Smith, J.A.; De Veaux, R.D. The Temporal and Spatial Variability of Rainfall Power. *Environmetrics* **1992**, *3*, 29–53. [CrossRef]
56. Fernández-Raga, M.; Rodríguez, I.; Caldevilla, P.; Búrdalo, G.; Ortiz, A.; Martínez-García, R. Optimization of a Laboratory Rainfall Simulator to Be Representative of Natural Rainfall. *Water* **2022**, *14*, 3831. [CrossRef]
57. Naves, J.; Anta, J.; Suárez, J.; Puertas, J. Development and Calibration of a New Dripper-Based Rainfall Simulator for Large-Scale Sediment Wash-Off Studies. *Water* **2020**, *12*, 152. [CrossRef]